

Final Draft
of the original manuscript:

Lu, X.; Blawert, C.; Tolnai, D.; Subroto, T.; Kainer, K.U.; Zhang, T.; Wang, F.; Zheludkevich, M.L.:

3D reconstruction of plasma electrolytic oxidation coatings on Mg alloy via synchrotron radiation tomography.

In: Corrosion Science. Vol. 139 (2018) 395 - 402.

First published online by Elsevier: May 16, 2018

DOI: /10.1016/j.corsci.2018.05.019

<https://dx.doi.org/10.1016/j.corsci.2018.05.019>

3D Reconstruction of Plasma Electrolytic Oxidation Coatings on Mg Alloy via Synchrotron Radiation Tomography

Xiaopeng Lu ^{a,b*}, Carsten Blawert ^b, Domonkos Tolnai ^b, Tungky Subroto ^b, Karl Ulrich Kainer ^b, Tao Zhang ^a, Fuhui Wang ^a, Mikhail L. Zheludkevich ^{b,c*}

^aCorrosion and Protection Division, Shenyang National Laboratory for Materials Science, Northeastern University, 3-11 Wenhua Road, Shenyang 110819, China

^bMagIC – Magnesium Innovation Centre, Institute of Materials Research, Helmholtz-Zentrum Geesthacht, Max-Planck-Str. 1, 21502 Geesthacht, Germany

^cFaculty of Engineering, University of Kiel, Kaiserstrasse 2, 24143 Kiel, Germany

*Corresponding author: luxiaopeng@mail.neu.edu.cn, mikhail.zheludkevich@hzg.de

Abstract: Plasma electrolytic oxidation (PEO) is a well-known surface treatment for Mg alloys, while high porosity is an issue to achieve long-term corrosion protection. Nevertheless, the presence of inherent porosity can be turned into advantage while used as nano/micro-structured reservoir of corrosion inhibitors or functional agents next to Mg surface providing an active corrosion protection and multi-functionality. For the first time, we report here the 3D internal architecture of PEO coated Mg via synchrotron-based microtomography. The pore characteristics have been qualitatively and quantitatively investigated to unveil the formation of the coating porosity and potential incorporation of functional elements in the pores.

Keywords: A: Magnesium; B: SEM; B: X-ray diffraction; C: Oxide coatings

1. Introduction

Mg and its alloys are attractive and promising metallic materials for various applications (e.g. automotive, aerospace and biomedical) due to excellent light-weight properties and biocompatibility [1-3]. However high chemical reactivity and poor corrosion performance are the main obstacles limiting their utilization in industrial and biomedical applications [4, 5]. Plasma electrolytic oxidation (PEO) is a well-recognized electrochemical surface treatment process to fabricate oxide coatings with enhanced corrosion and wear resistance [6-8]. PEO coated Mg generally demonstrates a high

porosity which decreases the long-term corrosion protection of the oxide coating [9, 10]. Nevertheless, the high porosity can be beneficial when the coatings are targeted at biomedical application as they are considered as degradable implants [11-14]. The developed porosity is also crucial when PEO coatings are modified to introduce additional functionalities to the treated surfaces. For example, addition of TiO₂ particles into the porous structure ensures superior photocatalytic properties to PEO coating formed on Mg alloy [15, 16]. Ex-situ incorporation of corrosion inhibitors are capable of providing active corrosion protection for the porous layer [13, 17-20]. Gnedenkov et al. [13, 18] found that filling the pores with 8-hydroxyquinoline could significantly improve the corrosion resistance of the coating. Corrosion inhibitors can be encapsulated into the open pores of PEO coating and subsequently sealed by sol-gel film to fabricate a high barrier composite coating to obtain superior protection against corrosion [17, 19]. In-situ incorporation of inhibitor containing nanocontainers has demonstrated to provide effective corrosion inhibition and self-healing properties for PEO coated Mg alloy [21, 22]. Therefore, basic understanding of characteristics and formation mechanism of the open pores are of vital importance to design PEO coatings for various potential applications. Investigation of the coating porosity is normally performed by means of microscopic analysis to observe the surface and cross-sectional microstructure and morphology of the coating [14, 23-26]. This methodology only demonstrates limited information and can be misleading occasionally since the real size and number of the pores is roughly estimated. The three-dimensional microstructure and geometry of the coating is hardly to be identified and investigated by the conventional microscopic analysis.

Synchrotron radiation microtomography is an unique non-destructive imaging tool applicable to materials because of the transversal coherence of the beam and high brilliance of the source [27-29]. In terms of Mg alloy, three-dimensional data provided by synchrotron based microtomography are applied to explore the internal architecture of the constituent phase and phase transformation. High resolution X-ray computed tomography has been recently utilized to qualitatively study the locations and morphologies of the pores on PEO coated titanium. It was reported that the porosity

constitutes 5.7% of the volume of PEO coating [30]. To the best of the authors' knowledge, there is no report regarding investigation of the 3D microstructure and porosity of PEO coatings on Mg and its alloys.

In the present study, synchrotron radiation tomography has been employed for the first time to reveal the three-dimensional microstructure and porosity of PEO coated AM50 Mg alloy. The characteristics of the open pores, i.e., size, volume and distribution, has been qualitatively and quantitatively investigated to disclose and understand the nature of the coating porosity. Our previous work [6, 31, 32] proved that oxide particles can be considered appropriate tracers to explore the formation mechanism of PEO coatings as they are incorporated into the layer along with the open pores. Consequently, inert rare-earth oxide particles (La_2O_3) are added to the electrolyte to study the evolution of the porosity during coating growth.

2. Material and Methods

The synchrotron radiation microtomography experiments were carried out at P05 (IBL) beamline of PETRA III, DESY (Deutsches Elektronen-Synchrotron), Germany. The accelerating energy was operated at 18 keV. The distance of the coating to the detector was 15 mm. During the acquisition of the tomograms, 1800 projections were taken with an acquisition time of 3s. The reconstructions resulted in volumes of $(960 \times 960 \times 1528)$ voxel with a voxel size of $(1.1 \mu\text{m})^3$. The spatial resolution of the reconstructed volumes was $2.9 \mu\text{m}$. The images obtained from the experiment were intensity-corrected by subtracting the original images with Gaussian-blur filtered images in image-processing software, Fiji [33]. Each tomographic volume was cropped and then filtered using Bilateral 3D filter to reduce noise while simultaneously preserving the edges. The segmentation started with a global thresholding followed by local 3D region-growing segmentations [34, 35].

AM50 Mg alloy were lathed to cylindrical specimens with average diameter of 1.2 mm and 6 mm in length. The elemental composition of the alloy is 4.74 wt.% Al, 0.383 wt.% Mn, 0.063 wt.% Si, 0.065 wt.% Zn, 0.002 wt.% Cu, 0.002 wt.% Fe and Mg balance, which was measured by an Arc Spark OES (Spark analyser M9, Spectro Ametek, Germany). A pulsed DC power supply was used to fabricate PEO coatings for 0.5, 1 and

10 min under a potentiostat mode (400 V). The applied duty ratio was 10% and frequency was 250 Hz. The electrolyte used to fabricate coatings is composed of Na₃PO₄ (30 g/L), KOH (1 g/L) and 5 g/L La₂O₃ particles (1-5 μm). The corresponding PEO coatings are named PEO_30 s, PEO_1 min and PEO_10 min, respectively. A mechanical stirring and bubbling system was applied to uniformly distribute particles in the electrolyte. The microstructure, morphology and elemental composition of the oxide coatings has been investigated by a scanning electron microscope (TESCAN Vega3 SB, Czech Republic).

3. Results and Discussion

The reconstructed 3D microstructure of the PEO coatings is demonstrated in Fig. 1. Red region corresponds to the distribution of the pores, while light blue color represents the inertly incorporated La₂O₃ particles in the layer. Table 1 shows quantitative analysis of the coating porosity as well as the number and volume of the pores/particles. It can be seen that the coating is quite porous at the early stage of the treatment (Fig. 1a and b), as reflected by the high volume of the open pores and high porosity (26.25 %, as shown in Table 1). The coating remains to be porous with the increase of treatment time, while a large number of La₂O₃ particles are observable in the coating treated for longer treatment time (Fig. c and e), suggesting that the uptake and incorporation of particles are accompanied by coating growth. With the prolongation of the treatment time, the total volume of the pores slightly decreases from $2.10 \times 10^7 \mu\text{m}^3$ to $1.75 \times 10^7 \mu\text{m}^3$ and $1.48 \times 10^7 \mu\text{m}^3$, while the pore number increases from 16025 to 21652 and 27868, respectively. As expected, the volume of the incorporated particles as well as the volume of the coating increases greatly with the growth of the layer. It is noteworthy that the increasing rate of the particle volume is much higher than that of the coating volume. The volume of the particles increases around 13 times after treated for 10 min, whereas the volume of the PEO coating has doubled from $5.85 \times 10^7 \mu\text{m}^3$ to $1.15 \times 10^8 \mu\text{m}^3$. In the case of the coating porosity, it decreases significantly from 26.25 % to 10.88 %. The obtained information is direct evidence to verify that PEO coated Mg is much more porous compared to the coating fabricated on other light metals, e.g., 5.7 % porosity for PEO coated Ti [30]. Nevertheless, the coating porosity primarily depends on the applied electrolyte and

electrical parameters during PEO process and the powder supply has a huge influence on the microstructure and properties of the coating.

The surface morphology of the coatings is additionally explored by scanning electron microscope (Fig. 2). The coating treated for longer time seems to be rougher and has more large-sized open pores compared to the coating obtained at the early stage. The cross-sectional microstructure and morphology of the PEO coatings has been investigated by means of traditional metallographic preparation to compare with the slicing obtained from the synchrotron tomography (Fig. 3). It is apparent that the coating thickness is proportional to the treatment time applied during PEO process. The oxide layers tend to be denser after metallographic preparation process (Fig. 3b, d and f). It is most likely that resin and coating debris generated during polishing process is embedded and preserved in the pores and defects, leading to an artificial denser and thicker layer. Many large-sized defects are found in the tomographic slicing (Fig. 3a, c and e), which is scarcely visible in the polished cross-sectional SEM images. The through-going defects indeed can have a very detrimental role in the barrier properties of the produced PEO coatings. According to the tomographic slicing, the large-sized defects are still observable for the coating treated for 10 min (Fig. 3e), indicating that the layer will continue to grow in these defective places due to dielectric breakdown of the coating. As for the particles (Fig. 4), they are incorporated into the layer from the beginning of the treatment. It can be seen that a large number of particles are agglomerated around the large-sized pores and defects in the coating (Fig. 4b and c). The majority of the particles are primarily located at the middle/inner part of the layer, suggesting that particles flow backwards with the melted material when the discharges are extinguished and remain at the defective place in the coating. Plenty of La enriched regions are observable in Fig. 4c, which is much larger than the original size of the La_2O_3 particles (Fig. 4d). It can be inferred that the incorporated particles are partially melted by the high intensity discharges in the later stage of PEO treatment. Additionally, the largest defect in the coating treated for 10 min is reconstructed to further understand the porosity and microstructure of PEO coating (Fig. 5). Intriguingly, several pores which are generally observed on the coating surface by SEM might derive from a single large pore/defect beneath the surface and even

connect to the inner part of the layer. It is truth that there is a continuous pore band between inner barrier layer and outer porous layer for PEO coatings produced from a phosphate-based electrolyte. The porous layer can be used as a high-volume depot for storing functional nanoparticles or active substances such as corrosion inhibitors to provide more functionalities for Mg surface. For instance, ex-situ incorporation of corrosion inhibitors by means of post-treatment is capable of enhancing the corrosion performance of PEO coating, while in-situ inert incorporation of inhibitor-containing nanocontainers can provide active corrosion protection and seal-healing property for long-term protection of Mg.

The geometry and volume of the detected pores and particles have been quantified to explore the evolution of the porosity and growth of the coating. The sphericity (Ψ) of the pores/particles in the coating is calculated by equation (1), where A_p is the surface area of the pores/particles and V_p is the volume of the pores/particles [36]. $\Psi=1$ is equivalent to a sphere and $\Psi=0$ represents an infinite plate. The distribution of the sphericity of the pores/particles in the coatings is shown in Fig. 6 and Fig. 7, respectively.

$$\Psi = \frac{\pi^{\frac{1}{3}}(6V_p)^{\frac{2}{3}}}{A_p} \quad (1)$$

The correlation between the sphericity and volume of the pores (Fig. 6) in coatings is influenced by the treatment time. The faction of high-sphericity pores in the range of $10^3 \mu\text{m}^3$ to $10^4 \mu\text{m}^3$ increases along with the coating growth, which is consistent with the evolution of number and volume of the pores in Table 1. The pore number increases with the coating thickness while the pore volume decreases with the treatment time, indicating that the irregular pores transform into more number of spheroid-like pores due to the newly formed coating material. Majority of the pores are below $10^4 \mu\text{m}^3$ with relatively high sphericity, while the large-sized pores generally show a low sphericity. Particularly, several highly irregular pores/defects with sphericity close to 0 are found in the coating. In the case of particles (Fig. 7), the number and volume increase greatly in proportion to the treatment time applied during PEO process. As expected, most of the incorporated particles are isolated in the coating at the early stage (Fig. 7a). The particles flow back with the melted material via discharge channel and agglomerate around pores and defects

with the growth of the layer, resulting in formation of a large fraction of large-sized particles with relatively low sphericity (Fig. 7c). In summary, synchrotron tomography is a high-efficiency technique to provide precise analysis of the coating porosity (volume, size and sphericity) and to disclose the 3D microstructure of PEO coating.

4. Conclusions

The evolution and distribution of the pores in PEO coated Mg has been revealed for the first time via synchrotron-based microtomography, which is of great importance to unveil the 3D internal architecture of the porous layer along with the coating growth. The characteristics of the pores has been qualitatively and quantitatively investigated to understand the microstructure and morphology of PEO coating. It is found that the coating porosity decreases with the growth of the layer under a potentiostat regime. The open pores on the coating surface might derive from one large pore/defect, which is hardly to be observed by means of conventional electron-microscopic analysis. A pore band has been proved to exist between the outer layer and inner barrier layer for PEO coatings produced from phosphate-based electrolyte. The inherent porosity of PEO coating has a good potential to be considered as efficient reservoir to store functional molecules to provide active corrosion protection and more functionalities for Mg surface.

Acknowledgements

The authors acknowledge the Deutsches Elektronen-Synchrotron for the provision of synchrotron radiation facilities within the framework of proposal I-20130105. The technical support of Dr. J. Herzen, Dr. M. Mohedano, Mr. R.H. Buzolin, Mr. V. Heitmann and Mr. U. Burmester is gratefully acknowledged. The authors would like to acknowledge the financial support of the National Natural Science Foundation of China (NO. U1737102, 51531007, 51771050), Young Elite Scientists Sponsorship Program of China Association for Science and Technology (2017QNRC001), Fundamental Research Funds for the Central Universities (N170203006 and N170205002) and National Program for Young Top-notch Professionals. This work in part was financed by the European project MULTISURF (Marie Skłodowska-Curie Research Program, grant agreement No 645676).

References

- [1] A. Pardo, M.C. Merino, A.E. Coy, R. Arrabal, F. Viejo, E. Matykina, Corrosion behaviour of magnesium/aluminium alloys in 3.5 wt.% NaCl, *Corrosion Science*, 50 (2008) 823-834.
- [2] S. Johnston, Z. Shi, A. Atrens, The influence of pH on the corrosion rate of high-purity Mg, AZ91 and ZE41 in bicarbonate buffered Hanks' solution, *Corrosion Science*, 101 (2015) 182-192.
- [3] Q. Tan, N. Mo, C.-L. Lin, B. Jiang, F. Pan, H. Huang, A. Atrens, M.-X. Zhang, Improved oxidation resistance of Mg-9Al-1Zn alloy microalloyed with 60 wt ppm Be attributed to the formation of a more protective (Mg,Be)O surface oxide, *Corrosion Science*, 132 (2018) 272-283.
- [4] S.V. Lamaka, B. Vaghefinazari, D. Mei, R.P. Petrauskas, D. Höche, M.L. Zheludkevich, Comprehensive screening of Mg corrosion inhibitors, *Corrosion Science*, 128 (2017) 224-240.
- [5] G. Duan, L. Yang, S. Liao, C. Zhang, X. Lu, Y. Yang, B. Zhang, Y. Wei, T. Zhang, B. Yu, X. Zhang, F. Wang, Designing for the chemical conversion coating with high corrosion resistance and low electrical contact resistance on AZ91D magnesium alloy, *Corrosion Science*, 135 (2018) 197-206.
- [6] X. Lu, C. Blawert, M.L. Zheludkevich, K.U. Kainer, Insights into plasma electrolytic oxidation treatment with particle addition, *Corrosion Science*, 101 (2015) 201-207.
- [7] K. Dong, Y. Song, D. Shan, E.-H. Han, Corrosion behavior of a self-sealing pore micro-arc oxidation film on AM60 magnesium alloy, *Corrosion Science*, 100 (2015) 275-283.
- [8] J. Yang, X. Lu, C. Blawert, S. Di, M.L. Zheludkevich, Microstructure and corrosion behavior of Ca/P coatings prepared on magnesium by plasma electrolytic oxidation, *Surface and Coatings Technology*, 319 (2017) 359-369.
- [9] X. Lu, M. Mohedano, C. Blawert, E. Matykina, R. Arrabal, K.U. Kainer, M.L. Zheludkevich, Plasma electrolytic oxidation coatings with particle additions – A review, *Surface and Coatings Technology*, 307, Part C (2016) 1165-1182.
- [10] M. Mohedano, R. Arrabal, B. Mingo, A. Pardo, E. Matykina, Role of particle type and concentration on characteristics of PEO coatings on AM50 magnesium alloy, *Surface and Coatings Technology*, 334 (2018) 328-335.
- [11] T.S.N. Sankara Narayanan, I.S. Park, M.H. Lee, Strategies to improve the corrosion resistance of microarc oxidation (MAO) coated magnesium alloys for degradable implants: Prospects and challenges, *Progress in Materials Science*, 60 (2014) 1-71.
- [12] L. Zhang, J. Zhang, C.-f. Chen, Y. Gu, Advances in microarc oxidation coated AZ31 Mg alloys for biomedical applications, *Corrosion Science*, 91 (2015) 7-28.
- [13] A.S. Gnedenkoy, S.L. Sinebryukhov, D.V. Mashtalyar, S.V. Gnedenkoy, Protective properties of inhibitor-containing composite coatings on a Mg alloy, *Corrosion Science*, 102 (2016) 348-354.
- [14] L.-Y. Cui, S.-D. Gao, P.-P. Li, R.-C. Zeng, F. Zhang, S.-Q. Li, E.-H. Han, Corrosion resistance of a self-healing micro-arc oxidation/polymethyltrimethoxysilane composite coating on magnesium alloy AZ31, *Corrosion Science*, 118 (2017) 84-95.

- [15] W. Li, M. Tang, L. Zhu, H. Liu, Formation of microarc oxidation coatings on magnesium alloy with photocatalytic performance, *Applied Surface Science*, 258 (2012) 10017-10021.
- [16] X. Lu, M. Schieda, C. Blawert, K.U. Kainer, M.L. Zheludkevich, Formation of photocatalytic plasma electrolytic oxidation coatings on magnesium alloy by incorporation of TiO₂ particles, *Surface and Coatings Technology*, 307, Part A (2016) 287-291.
- [17] S.V. Lamaka, G. Knörnschild, D.V. Snihirova, M.G. Taryba, M.L. Zheludkevich, M.G.S. Ferreira, Complex anticorrosion coating for ZK30 magnesium alloy, *Electrochimica Acta*, 55 (2009) 131-141.
- [18] A.S. Gnedenkov, S.L. Sinebryukhov, D.V. Mashtalyar, S.V. Gnedenkov, Localized corrosion of the Mg alloys with inhibitor-containing coatings: SVET and SIET studies, *Corrosion Science*, 102 (2016) 269-278.
- [19] D.K. Ivanou, K.A. Yasakau, S. Kallip, A.D. Lisenkov, M. Starykevich, S.V. Lamaka, M.G.S. Ferreira, M.L. Zheludkevich, Active corrosion protection coating for a ZE41 magnesium alloy created by combining PEO and sol-gel techniques, *RSC Advances*, 6 (2016) 12553-12560.
- [20] M. Serdechnova, M. Mohedano, B. Kuznetsov, C.L. Mendis, M. Starykevich, S. Karpushenkov, J. Tedim, M.G.S. Ferreira, C. Blawert, M.L. Zheludkevich, PEO Coatings with Active Protection Based on In-Situ Formed LDH-Nanocontainers, *J Electrochem Soc*, 164 (2017) C36-C45.
- [21] M. Sun, A. Yerokhin, M.Y. Bychkova, D.V. Shtansky, E.A. Levashov, A. Matthews, Self-healing plasma electrolytic oxidation coatings doped with benzotriazole loaded halloysite nanotubes on AM50 magnesium alloy, *Corrosion Science*, 111 (2016) 753-769.
- [22] M. Mohedano, X. Lu, E. Matykina, C. Blawert, R. Arrabal, M.L. Zheludkevich, Plasma Electrolytic Oxidation (PEO) of Metals and Alloys, in: *Reference Module in Chemistry, Molecular Sciences and Chemical Engineering*, Elsevier, 2017.
- [23] L. Yu, J. Cao, Y. Cheng, An improvement of the wear and corrosion resistances of AZ31 magnesium alloy by plasma electrolytic oxidation in a silicate-hexametaphosphate electrolyte with the suspension of SiC nanoparticles, *Surface and Coatings Technology*, 276 (2015) 266-278.
- [24] S.V. Gnedenkov, S.L. Sinebryukhov, D.V. Mashtalyar, K.V. Nadaraia, A.S. Gnedenkov, V.M. Bouzник, Composite fluoropolymer coatings on the MA8 magnesium alloy surface, *Corrosion Science*, 111 (2016) 175-185.
- [25] S. Stojadinović, N. Tadić, N. Radić, B. Grbić, R. Vasilić, MgO/ZnO coatings formed on magnesium alloy AZ31 by plasma electrolytic oxidation: Structural, photoluminescence and photocatalytic investigation, *Surface and Coatings Technology*, 310 (2017) 98-105.
- [26] Y. Chen, X. Lu, C. Blawert, M.L. Zheludkevich, T. Zhang, F. Wang, Formation of self-lubricating PEO coating via in-situ incorporation of PTFE particles, *Surface and Coatings Technology*, 337 (2018) 379-388.

- [27] D. Tolnai, G. Requena, P. Cloetens, J. Lendvai, H.P. Degischer, Sub-micrometre holotomographic characterisation of the effects of solution heat treatment on an AlMg7.3Si3.5 alloy, *Materials Science and Engineering: A*, 550 (2012) 214-221.
- [28] E. Maire, P.J. Withers, Quantitative X-ray tomography, *International Materials Reviews*, 59 (2014) 1-43.
- [29] G. Garces, D.G. Morris, M.A. Muñoz-Morris, P. Perez, D. Tolnai, C. Mendis, A. Stark, H.K. Lim, S. Kim, N. Shell, P. Adeva, Plasticity analysis by synchrotron radiation in a Mg₉₇Y₂Zn₁ alloy with bimodal grain structure and containing LPSO phase, *Acta Materialia*, 94 (2015) 78-86.
- [30] X. Zhang, S. Aliasghari, A. Němcová, T.L. Burnett, I. Kuběna, M. Šmíd, G.E. Thompson, P. Skeldon, P.J. Withers, X-ray Computed Tomographic Investigation of the Porosity and Morphology of Plasma Electrolytic Oxidation Coatings, *ACS Applied Materials & Interfaces*, 8 (2016) 8801-8810.
- [31] X. Lu, C. Blawert, K.U. Kainer, M.L. Zheludkevich, Investigation of the formation mechanisms of plasma electrolytic oxidation coatings on Mg alloy AM50 using particles, *Electrochimica Acta*, 196 (2016) 680-691.
- [32] X. Lu, C. Blawert, Y. Huang, H. Ovri, M.L. Zheludkevich, K.U. Kainer, Plasma electrolytic oxidation coatings on Mg alloy with addition of SiO₂ particles, *Electrochimica Acta*, 187 (2016) 20-33.
- [33] J. Schindelin, I. Arganda-Carreras, E. Frise, V. Kaynig, M. Longair, T. Pietzsch, S. Preibisch, C. Rueden, S. Saalfeld, B. Schmid, J.-Y. Tinevez, D.J. White, V. Hartenstein, K. Eliceiri, P. Tomancak, A. Cardona, Fiji: an open-source platform for biological-image analysis, *Nature Methods*, 9 (2012) 676.
- [34] A. Manduca, L. Yu, D. Trzasko Joshua, N. Khaylova, M. Kofler James, M. McCollough Cynthia, G. Fletcher Joel, Projection space denoising with bilateral filtering and CT noise modeling for dose reduction in CT, *Medical Physics*, 36 (2009) 4911-4919.
- [35] T. Subroto, C.L. Mendis, F. D'Elia, G. Szakács, J.L. Fife, N. Hort, K.U. Kainer, D. Tolnai, 3D Microstructural Evolution on Solidifying Mg–5Nd–5Zn Alloy Observed via In Situ Synchrotron Tomography, in: K.N. Solanki, D. Orlov, A. Singh, N.R. Neelameggham (Eds.) *Magnesium Technology 2017*, Springer International Publishing, Cham, 2017, pp. 605-612.
- [36] H. Wadell, Volume, Shape, and Roundness of Quartz Particles, *The Journal of Geology*, 43 (1935) 250-280.

Figure Caption:

Fig. 1. Distribution of the pores (in red) and particles (in light blue) in the coatings. (a and b) PEO_30 s, (c and d) PEO_1 min, (e and f) PEO_10 min.

Fig. 2. Surface morphology of the coatings obtained from SEM. (a) PEO_30 s, (b) PEO_1 min, (c) PEO_10 min.

Fig. 3. Coating morphology obtained from tomographic slicing (a) PEO_30s, (c) PEO_1 min, (e) PEO_10 min. SEM cross-sectional morphology of the coatings by means of conventional metallographic preparation (b) PEO_30s, (d) PEO_1 min, (f) PEO_10 min.

Fig. 4. EDS mapping of the coatings (a) PEO_30s, (b) PEO_1 min, (c) PEO_10 min; (d) La_2O_3 particle morphology.

Fig. 5. 3D reconstruction of the largest pore in the coating treated for 10 min.

Fig. 6. Sphericity distribution of the individual pores in the coatings.

Fig. 7. Sphericity distribution of the individual particles in the coatings.

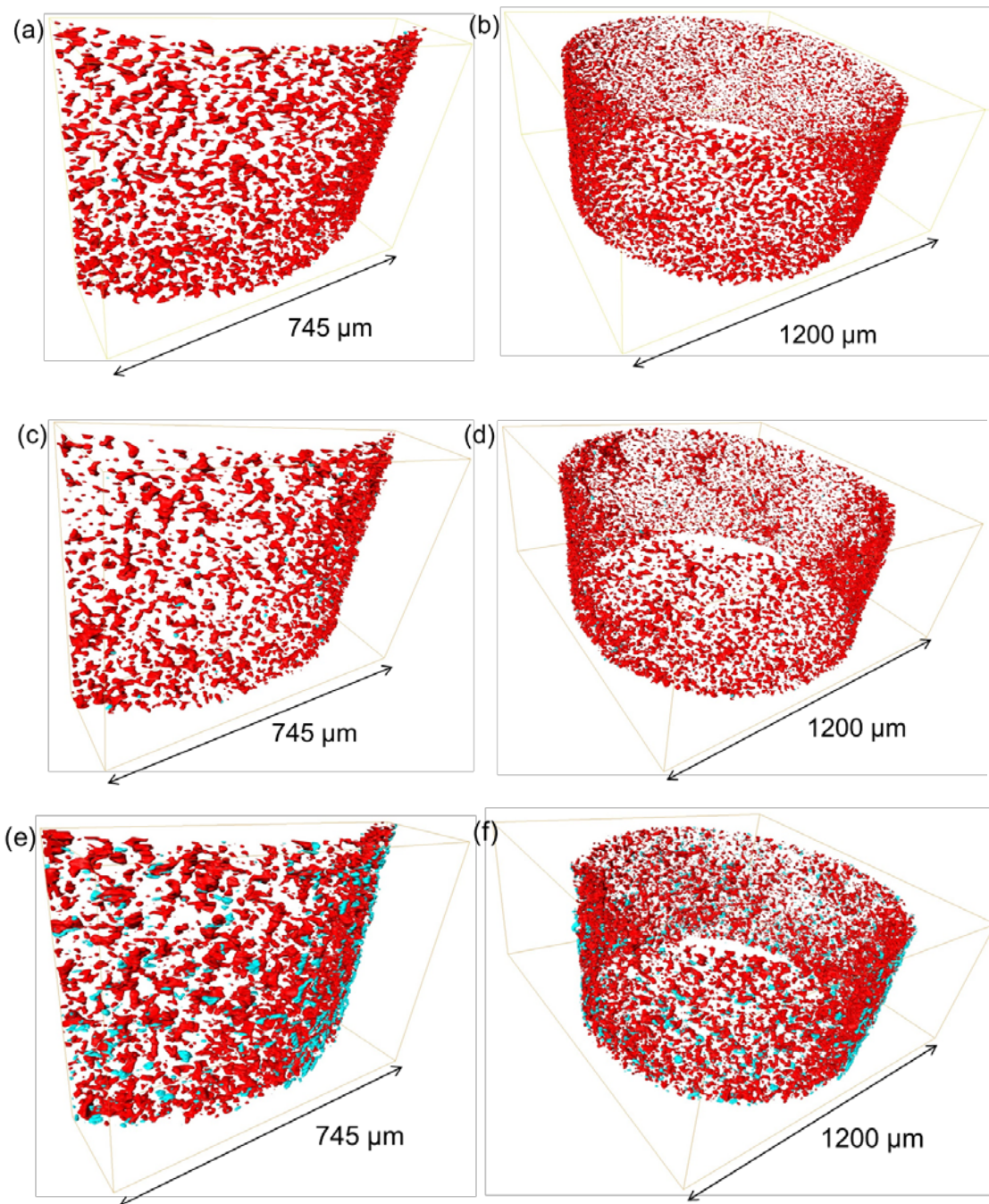


Figure 1

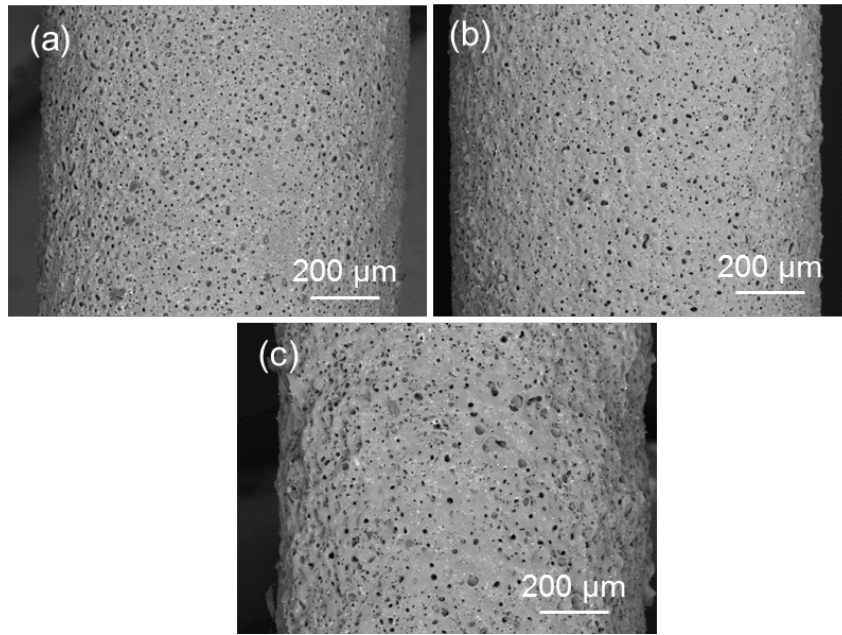


Figure 2

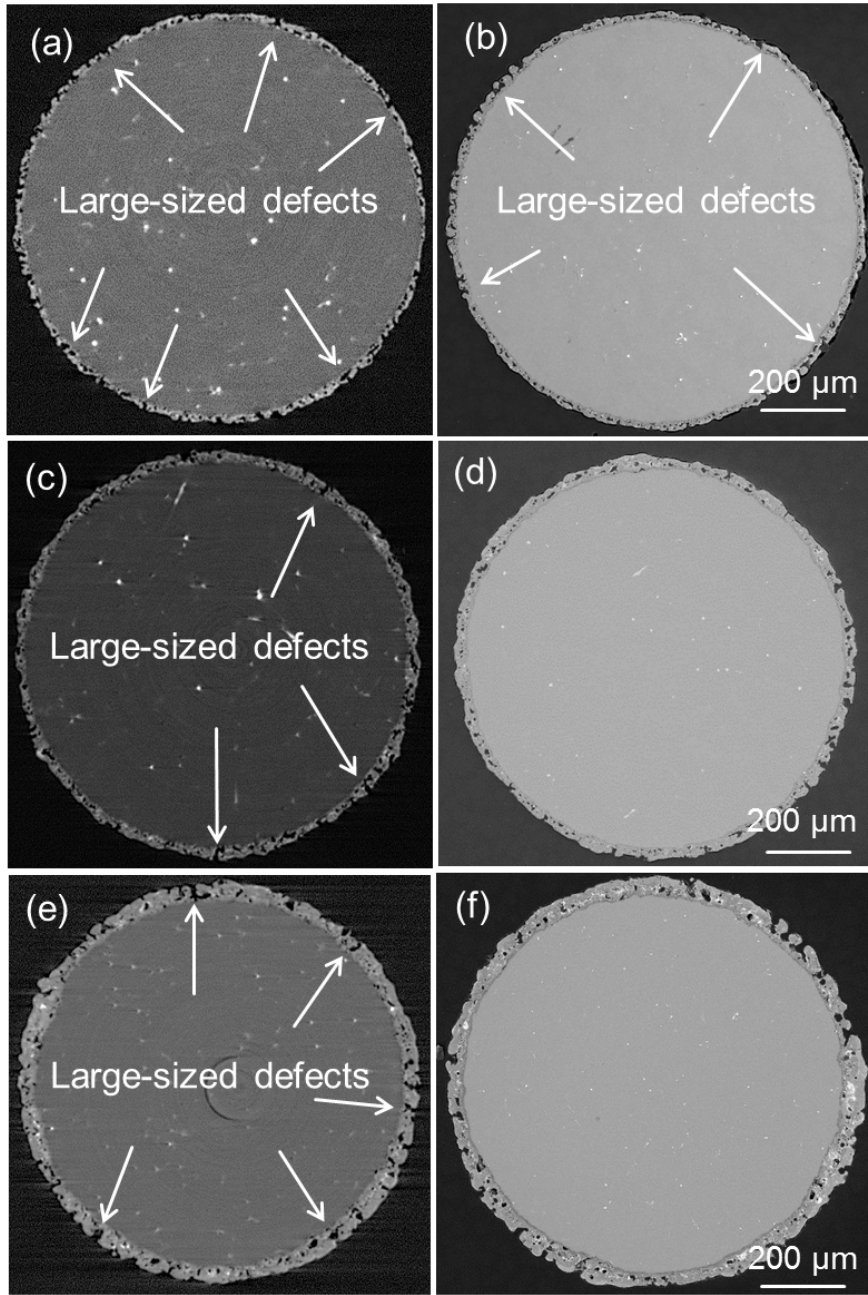


Figure 3

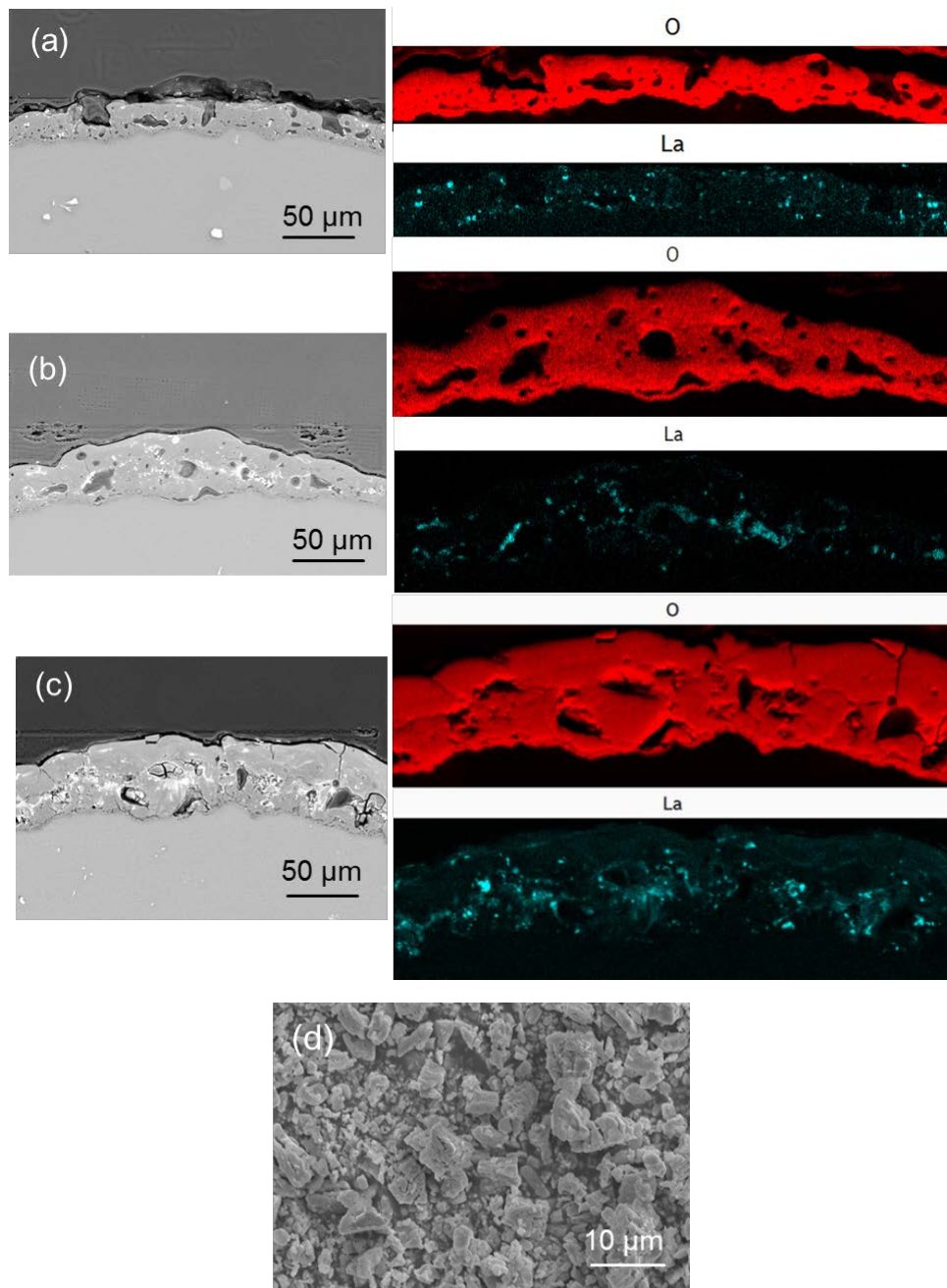


Figure 4

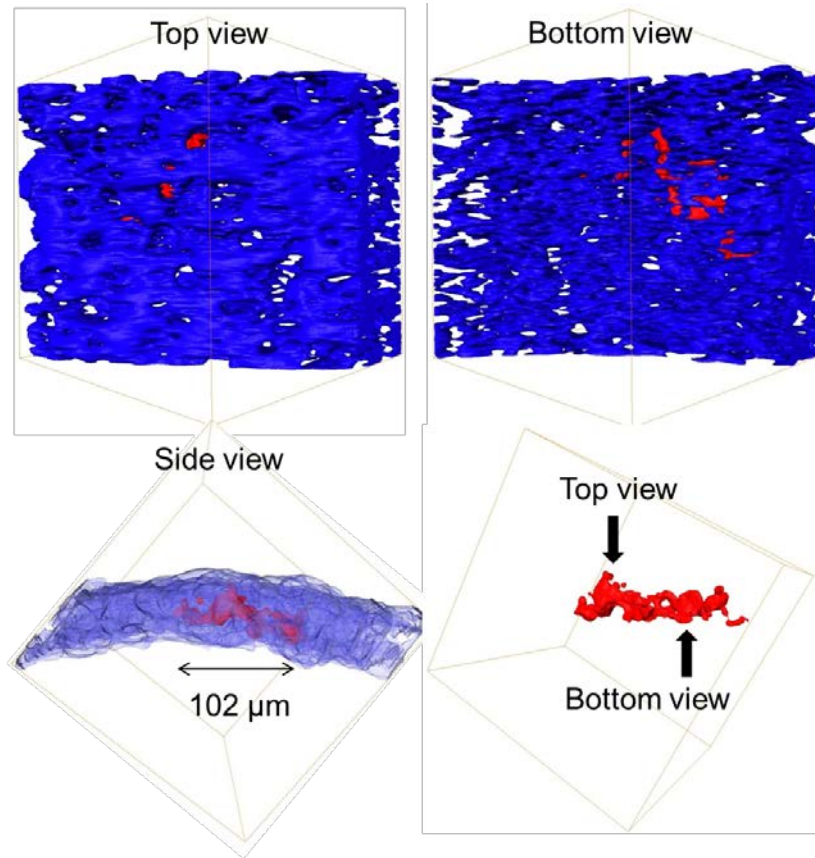


Figure 5

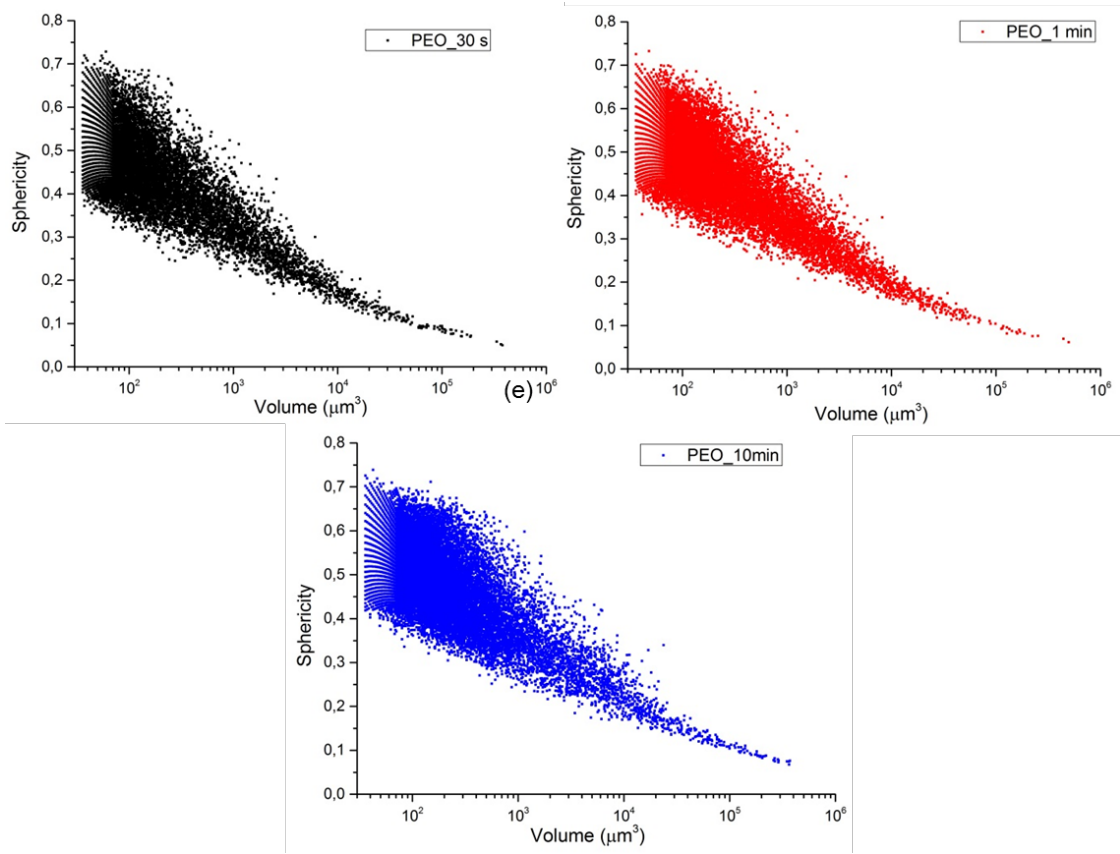


Figure 6

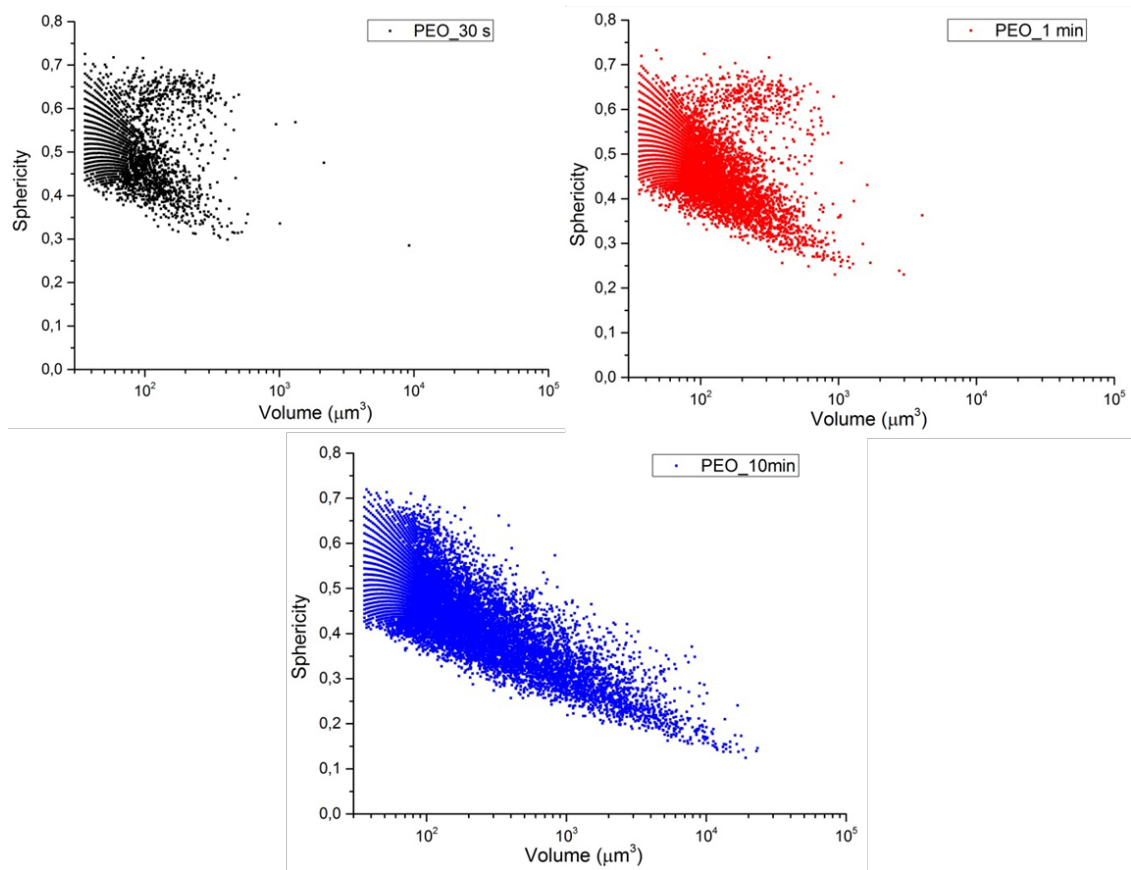


Figure 7

Table 1. Volume of the pores, particles and the coating in **Figure 1**.

Coating	Volume and number of the pores	Volume and number of the particles	Volume of the produced coating	Porosity
PEO_30 s	$2.10 \times 10^7 \mu\text{m}^3$, 16025	$4.90 \times 10^5 \mu\text{m}^3$, 3760	$5.85 \times 10^7 \mu\text{m}^3$	26.25 %
PEO_1 min	$1.75 \times 10^7 \mu\text{m}^3$, 21652	$1.43 \times 10^6 \mu\text{m}^3$, 10350	$9.05 \times 10^7 \mu\text{m}^3$	15.99 %
PEO_10 min	$1.48 \times 10^7 \mu\text{m}^3$, 27868	$6.25 \times 10^6 \mu\text{m}^3$, 17603	$1.15 \times 10^8 \mu\text{m}^3$	10.88 %